Computational Analysis of Planned High-Speed Swept Wing-Elevon Experiments

Robert Alviani,* Gregory Blaisdell,† and Jonathan Poggie‡
Purdue University, West Lafayette, IN, 47907

A computational investigation of a high-speed swept wing-elevon model, which is to be used in upcoming experiments, is presented in this paper. This investigation was done in coordination with a planned experimental study to be conducted at Purdue University's Mach 6 quiet wind tunnel, with complementary experiments to be done at the University of Tennessee Space Institute's Mach 4 Ludwieg Tube. The purpose of this computational campaign was to aid experimentalists in understanding the general flow structure before running experiments. Turbulence was modeled with improved delayed detached-eddy simulation (IDDES). The focus of this paper is on visualization of the flow around the swept wing-elevon model and the resultant aerothermal loading. This flow exhibits features of several canonical flows, such as a fin interaction at the wing-root and a compression ramp interaction resulting from the elevon deflection. This specific model and flow configuration produce a large region of separation on the elevon's leeward side, which is related to several gaps around the wing-elevon juncture, including the cove region. The concomitant vortex produces streaks of high heat flux on the leeward surface, which generally has low levels of heat flux. The heat flux on the windward side is high because of flow reattachment and boundary layer thinning.

Nomenclature

C_f = Skin friction coefficient
D = Leading-edge diameter
f_s = Sampling frequency
L_r = Streak length
M = Mach number
P = Pressure
Re = Reynolds number
s = Running length
T = Temperature
α = Angle of attack
δ_f = Elevon deflection
δ = Boundary layer thickness
δ^* = Displacement thickness
Δ = Detached bow-shock distance

Subscripts
o = Stagnation
∞ = Freestream

I. Introduction

Research on shock-wave / boundary-layer interaction (SBLI) [1] has practical applications in the development of high-speed vehicle structures. Large elevon deflection on a wing-elevon body will cause strong SBLI and can lead

*Graduate Student, School of Aeronautics and Astronautics, Student Member AIAA.
†Professor, School of Aeronautics and Astronautics, AIAA Associate Fellow.
‡Professor, School of Aeronautics and Astronautics, AIAA Associate Fellow.

to significant aerothermodynamic loading. Geometric imperfections, such as protuberances or gaps, can introduce complex flow structures and vortices which also can increase aerothermal heating [2–8]. This joint computational and experimental project involves analyzing the complex high-speed flow around a swept wing-elevon model, focusing on regions where there is significant SBLI and vortex formation. Specific regions of interest include the wing-tip, the wing-root, the juncture of the wing's trailing-edge and elevon, where the cove is situated, and the wake. The cove is defined as the area between the wing's trailing-edge and elevon which is required to allow for elevon deflection. These regions produce high levels of heat transfer, such as on the deflected elevon surface, and intricate vortex formation, such as at the wing-tip and gap regions. Previous computations and analyses have been completed by the authors for high-speed flow over a similar geometry [9, 10]. Experiments for this swept wing-elevon model will be conducted with the Mach 6 quiet wind tunnel at Purdue University, and complementary experiments will be conducted with the University of Tennessee Space Institute's Mach 4 Ludwieg Tube. At this time, only blockage tests have been completed by the experimental team, allowing for a small amount of experimental data to be included in this paper. This paper presents computational analysis of the swept wing-elevon model, with flow conditions corresponding to Purdue's Mach 6 quiet wind tunnel.

II. Methodology

The swept wing-elevon model analyzed for this project was designed by Carson Lay at Purdue University. An isometric view of the model is provided in Figure 1, and the side and front profiles are provided in Figure 2. The model consists of a three-dimensional swept-wing, with an elevon attached to the trailing-edge. The elevon is deflected 12 deg. Between the wing and elevon are three gap regions. The primary gap region is the cove, and there are two additional side gaps. The swept wing-elevon model will be placed on the floor of the Purdue Mach 6 wind tunnel, which will act as a representative fuselage for the wing. The floor of the wind tunnel is represented by a 0.66 m flat plate so that the boundary layer can grow to match the corresponding wind tunnel displacement thickness, $\delta^* = 5.8$ mm, at the beginning of the model. The wing has a constant sweep of 25 deg from the z-axis. The airfoil cross-section of the wing consists of two straight ramped sections connected by a flat section. The airfoil is symmetric about its chord-line. Due to the swept leading-edge, the chord lengths of the airfoil cross-sections decrease from the root to the tip. The root cord length of the swept wing-elevon model is 0.423 m, the centerline chord length is 0.379 m, and the tip chord length is 0.334 m. The chord length of the elevon alone is 0.1 m and constant. The elevon is also symmetric about its chord-line. The span of the wing is 0.19 m, and the span of the elevon is 0.135 m. The cove region and the side gaps consist of constant-length regions between the wing and elevon of 2.52 mm. The cove region is created by two concentric circles about a center of rotation located in the cylindrical elevon's leading-edge (x,y,z) = (0.3275,0,0) m. The radius of curvature of the concave wing-cove surface is 8.15 mm. The radius of curvature of the convex elevon-cove surface is 5.63 mm. The leading-edge of the wing and the trailing-edges of the wing and elevon are all blunt with diameter of D = 850 μm.

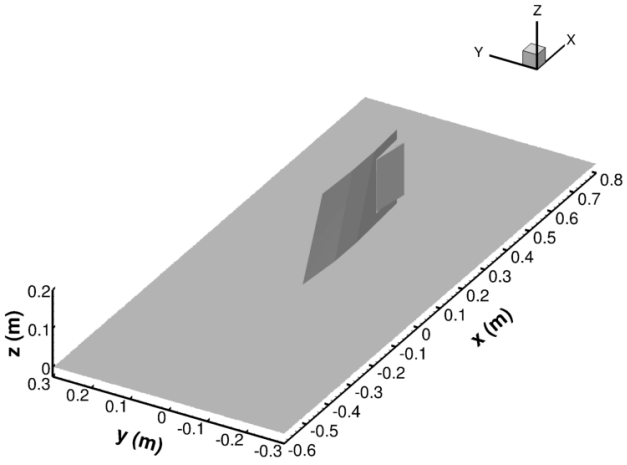

Fig. 1 Three-dimensional perspective of the swept wing-elevon model on the wind tunnel floor.

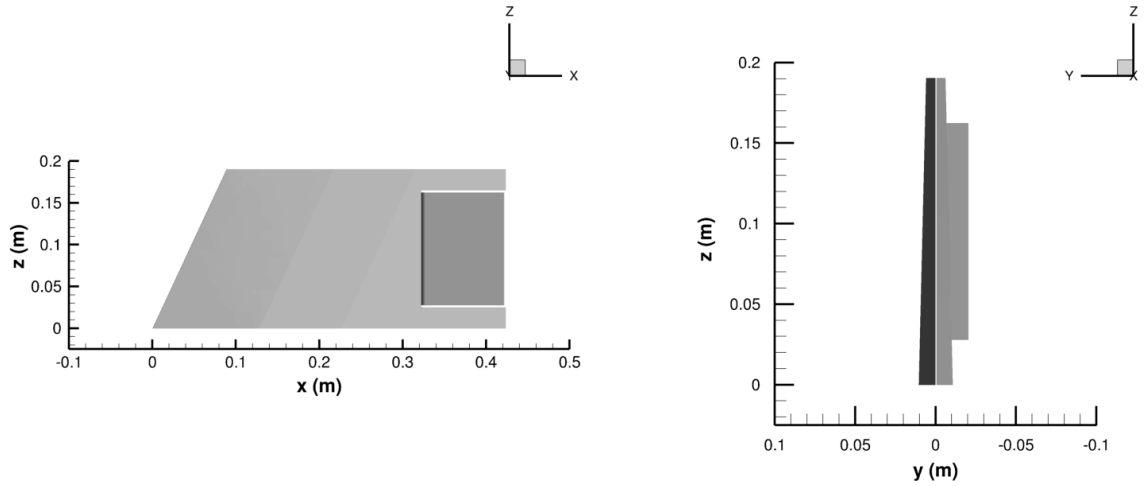

(a) Side profile **(b) Front profile**

Fig. 2 Side and front profiles of the swept wing-elevon model.

The flow conditions correspond to fully turbulent, Mach 6, high Reynolds number flow at zero angle of attack. Freestream conditions, and selected properties, are provided below in Table 1. Computational data were acquired with the CFD software CREATE-AV Kestrel KCFD, which is a finite volume method (FVM) solver. The mesh was produced with the commercial grid creation software Pointwise. The unstructured computational mesh comprised 250 million cell-volumes. The mesh was created with T-Rex hybrid unstructured meshing, allowing for high levels of resolution where needed. Post-processing of data was done using the software Tecplot. Turbulence was modeled with improved delayed detached-eddy simulation (IDDES), which utilizes both the Reynolds-averaged Navier-Stokes (RANS) equations and large-eddy simulation (LES) [11]. The RANS turbulence model used was Spalart-Allmaras. Spatial accuracy was second-order. The inviscid flux scheme was HLLE++, and the viscous flux scheme was LDD+. Temporal accuracy was second-order, achieved by a subiterative point-implicit scheme [12]. Model surface boundary conditions were set as no-slip cold, $T_w = 293.15$ K, isothermal surfaces. Boundary conditions in the spanwise direction were periodic. All other domain boundaries used a modified Riemann invariant boundary condition. The time step was $\Delta t = 1 \times 10^{-7}$ s. Results presented are averaged over time, at a frequency of every 10 iterations, or $f_s = 1 \times 10^{-6}$ Hz. Time-averaging was done after 3 ms to avoid including transient phenomena in the data collection. The total number of iterations was 200,000, resulting in a simulated time of 20 ms. The working gas was air, and assumed to be thermally, $p = \rho RT$, and calorically, $e = C_v T$, perfect. Computational resources were provided by the U.S. Navy high-performance computing (HPC) cluster Narwhal. Narwhal used 2.6-GHz AMD Epyc 7H12 processors, which have 64 cores per CPU, with 2 CPUs per node. The computation employed 75 nodes, for a total of 9600 cores, taking roughly 200 hours to run to completion.

Table 1 Freestream conditions and selected properties

Parameter	Value
M_∞	6
$T_{o,\infty}$ (K)	433
$P_{o,\infty}$ (kPa)	1034
Re_∞ (m^{-1})	1.1×10^7
δ_f (deg)	12
α (deg)	0

III. Results

The presented analysis in this paper focuses on flow visualization around the swept wing-elevon, the cove region, and the separation region on the trailing-edge of the elevon. In addition, the resultant surface aerothermal loading on the swept wing-elevon surface is also analyzed. Time-averaged flow visualization allows for enhanced insight into the complex flow interactions at different locations on the swept wing-elevon. In this section, the centerline plane of the swept wing-elevon model refers to a z-normal, x-y plane, which displays the center-most (z= 0.095 m) airfoil cross-section of the swept wing-elevon model. In addition, the center-thickness plane of the swept wing-elevon model refers to a y-normal, x-z plane, which cuts the model directly in half (y=0 m) about the center of the airfoil cross-section. All the data presented is time-averaged mean flow data.

The structure of data presentation is as follows. First, general flow visualization is provided. The fin interaction at the wing-root is visualized with use of three-dimensional streamlines. The general flow across the center-thickness plane and the centerline plane is visualized with two-dimensional Mach contours. The complex flow in the cove region and at the trailing edge of the elevon is further visualized with sectional streamlines. After, the aerothermal heating on the swept wing-elevon surface is provided. The swept wing-elevon and wind tunnel floor surface heating is visualized with a three-dimensional perspective view of the surface heat flux contours. The heating on both sides of the swept wing-elevon model is further visualized with side profile heat flux contours. Heating along the chord of the swept wing-elevon model is analyzed at various z-locations. In addition, heating across the span of the cove and the downstream elevon is also analyzed. The last portion of the results focuses on the intricate vortex formation at the wing-tip and on the leeward elevon surface. The heating on the leeward elevon surface is visualized with a local heat flux contour, and the heat flux along streaks that develop near the wing-tip and on the elevon surface are plotted. The wing-tip vortex is analyzed with use of surface skin friction trajectories, and an experimental photograph is provided for comparison. Lastly, three-dimensional streamlines and surface skin friction trajectories on the leeward elevon surface are provided to display the complex vortex formation observed.

A. Flow Visualization

The high-speed flow around the swept wing-elevon is three-dimensional and intricate. Leading up to the leading-edge of the wing, the incoming flow develops a turbulent boundary layer on the flat plate, which represents the wind tunnel floor. The boundary layer thickness at the start of the leading-edge is δ = 9.2 mm. The leading-edge diameter to boundary-layer thickness ratio is D/δ = 10.8. The boundary layer separates 1.9 mm (2.25 D) ahead of the wing-root symmetry line. The height of the separation vortex at the leading-edge symmetry line is 1.4 mm (1.65 D). This separation produces a horseshoe vortex that extends along the surface of the flat plate. In addition to this horseshoe vortex, a secondary vortex is seen forming closer to the swept wing-elevon surface. This behavior is typical for a high-speed fin interaction [13–15]. The structures of the horseshoe and secondary vortices are displayed in Figure 3, with streamlines colored by Mach number. In this figure, separation can be seen near the wing-root. The larger primary horseshoe vortex is seen propagating downstream of the fin. The majority of boundary layer flow redirects at the leading-edge and flows around the wing. The flow near the wing-root, along the floor, produces the secondary vortex that starts to creep up along the side of the wing.

Figure 4 provides flow visualization for both the centerline and center-thickness planes with Mach contours. For the center-thickness plane (left), the elevon is protruding out-of-the-page. The incoming turbulent boundary layer separates near the wing-root, as shown in Figure 3, and flows downstream of the wing's leading-edge. The leading-edge produces a detached bow-shock in the inviscid freestream flow region, creating a small layer of subsonic flow. The average detached bow-shock distance, Δ, is roughly 300 μm (0.35 D). This produces extremely high heat transfer, similar to a blunt-body flow [16, 17]. The flow produces a low-momentum layer around the wing-tip, along with a weak Mach wave created by the flow turning around the leading-edge of the wing. The wake of the swept wing-elevon model involves regions of low-speed subsonic flow near the edges of the wing-tip and wing-root, as well as regions of high speed flow expanding in the wake of the leeward side of the elevon. Although hard to see in this figure, the flow in the cove is mostly subsonic, with small regions of supersonic flow.

Figure 4b displays the flow over the swept wing-elevon centerline, at z = 0.095 m, which resembles a generic high-speed airfoil with a deflected elevon. Here, the wing-elevon surface extends both into and out-of-the-page, and the viewpoint is looking upwards from the wind tunnel floor. There is a leading-edge detached bow-shock that propagates downstream. A thick low-momentum layer develops on the top and bottom of the airfoil leading up to the wing-elevon cove region. Outside of the incoming turbulent boundary layer, the flow along the wing, before the elevon, is symmetric about the centerline because the wing airfoil is symmetric. The elevon deflection, 12 deg, creates a strong SBLI as the

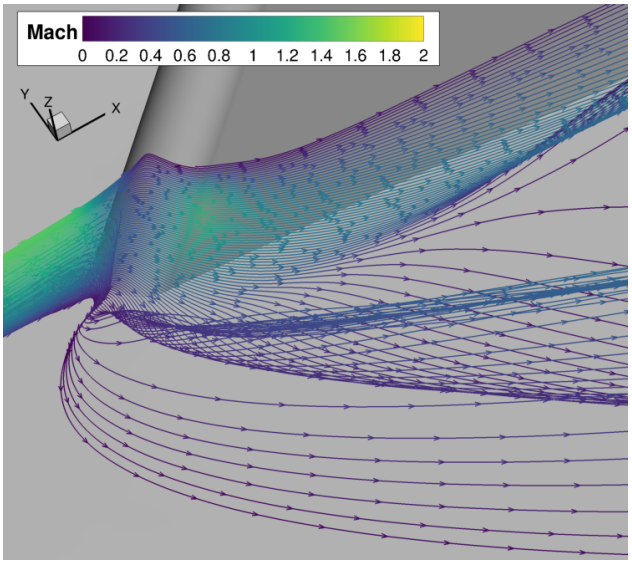

Fig. 3 Three-dimensional flow streamlines at wing-root.

reattaching wing boundary layer is abruptly deflected upwards. For this deflection, the flow on the leeward side of the elevon separates, creating a large region of separation. There is a small amount of flow through the cove, which may contribute to this separation; the flow through the cove and the elevon separation is shown more clearly in Figure 5a. Flow structures along airfoil sections which include the elevon are all nearly identical to the flow shown in Figure 4b.

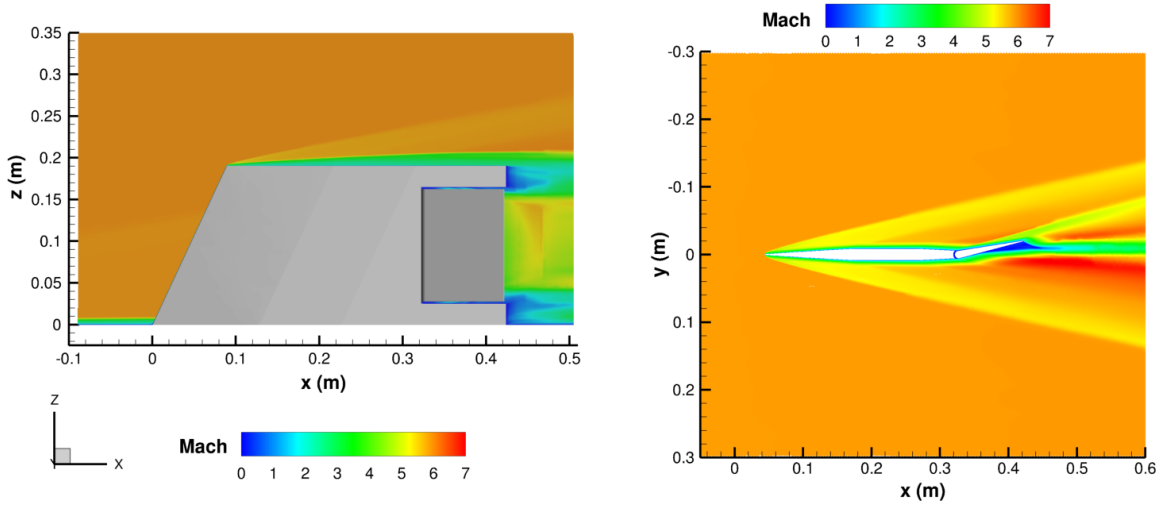

(a) Center-thickness plane **(b) Centerline plane**

Fig. 4 Mach contours of flow around the swept wing-elevon model.

Sectional streamlines in the cove region and at the elevon trailing-edge are displayed in Figure 5. The streamlines are taken from the swept wing-elevon centerline, z = 0.095 m. As the boundary layer separates from the wing surface, a separation region is formed attached to the wing surface, displayed in Figure 5a. Slightly downstream of this separation vortex, flow turns and continues into the cove, flows through the cove, and exits on the leeward side of the elevon. This behavior is expected from previous wing-elevon cove computations [9, 10] and experiments [18]. There are two more vortices that form inside of the cove, both attached to the elevon surface. This structure is very similar throughout the span of the wing-elevon cove. Figure 5b shows the separation region on the leeward elevon surface. The separation region is large, spanning about 60% of the elevon surface. There is a secondary separation vortex that is also seen near

the primary region of separation. The primary region of separation is caused both in part by flow exiting the cove from the windward surface and from the intricate vortex formation produced by entrainment of the side gap flow.

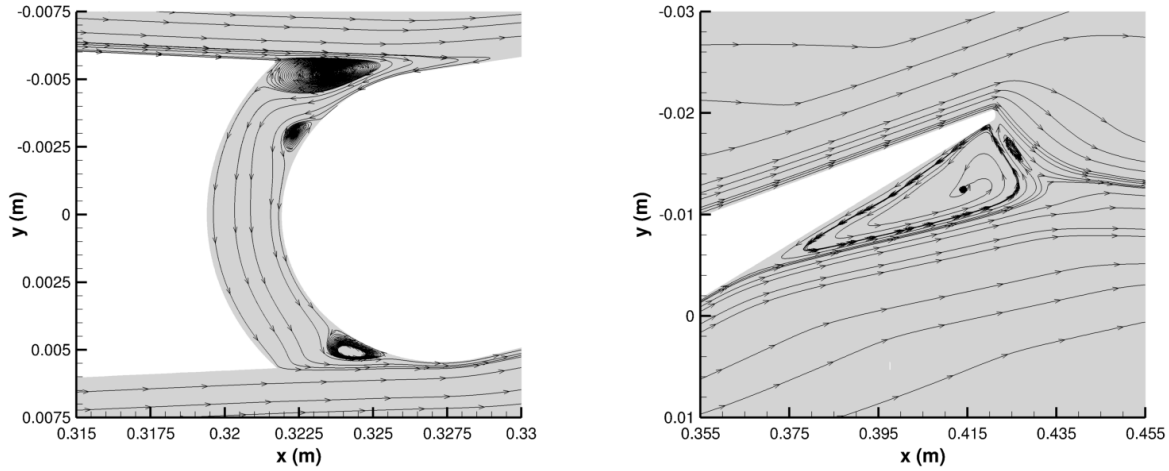

(a) Cove region **(b) Elevon trailing-edge**

Fig. 5 Sectional streamlines in the cove region and near the elevon trailing-edge.

B. Aerothermal Heating

One of the primary interests in high-speed flow is the high rates of heat transfer. Below, in Figure 6, a three-dimensional perspective view of the surface heat flux is shown. As mentioned previously, the highest levels of heat flux are on the leading-edge of the wing. As the boundary layer grows along the wing surface, the heat flux decreases as expected. On the elevon windward surface, which is outward facing in this figure, there is a large amount of aerothermal heating produced from the strong SBLI. On the surface of the flat plate, or the wind tunnel floor, there is aerothermal heating around the swept wing-elevon model that is produced by the horseshoe vortex in the wake of the fin interaction. A small region of high heat flux is seen on the floor, near the flat portion of the wing, where the secondary vortex moves from the floor up along the wing surface. The diverted flow from the deflected elevon also produces heat flux on the floor, in a similar shape to the general flow structure shown in Figure 4b.

Heat flux on both the windward and leeward wing-elevon surface are displayed in Figure 7. The high heat flux at the wing's leading-edge is seen clearly here. After the leading-edge, the turbulent boundary layer starts to develop, and the reduction in heat flux along the wing surface can be seen. The influence of the wing-root interaction is seen at the bottom of the wing, starting at the flat portion of the wing surface, around x = 0.13 m. At the wing-elevon juncture, the boundary layer on the wing separates momentarily due to the cove gap region. The boundary layer reattaches onto the elevon surface and becomes much thinner, creating higher heat flux on the windward elevon surface, shown in Figure 7a. The SBLI created by the 12 deg elevon deflection produces high heat transfer slightly downstream on the elevon surface. The asymmetric heat flux about in the spanwise direction is caused by the various boundary layer thicknesses along the spanwise surface. The boundary layer is thinner at the wing-tip than the wing-root, thus the heat flux is higher near the wing-tip than near the wing-root. On the upper and lower portions of the side gaps, there are two regions of high heat flux caused by flow turning into the gap region from the side of the wing. There is also a large heat flux streak on the top of both sides of the wing, caused by the formation of a wing-tip vortex. On the leeward side of the elevon, shown in Figure 7b, two large streaks are seen, associated with the presence of additional vortices.

The heat flux along the chord of the swept wing-elevon is plotted in Figure 8. Figure 8a displays heat flux at different z-locations on the model, only on the windward surface. The leading-edge of the swept wing-elevon model produces the highest levels of heat flux. Since no transition model was employed, the boundary layer immediately transitions to turbulence, which is associated with the local minimum. At each of the segmental turns along the wing, the heat flux peaks momentarily, then continues to drop as the boundary layer thickens. The cove is located at around x = 0.32 m, which is where the large drop in heat flux occurs. The flow reattaches on the elevon quickly, and the heat flux continues

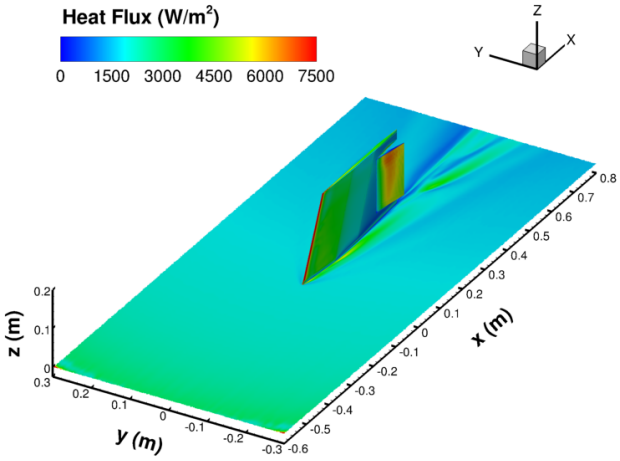

Fig. 6 Three-dimensional perspective of the swept wing-elevon model surface heat flux contours.

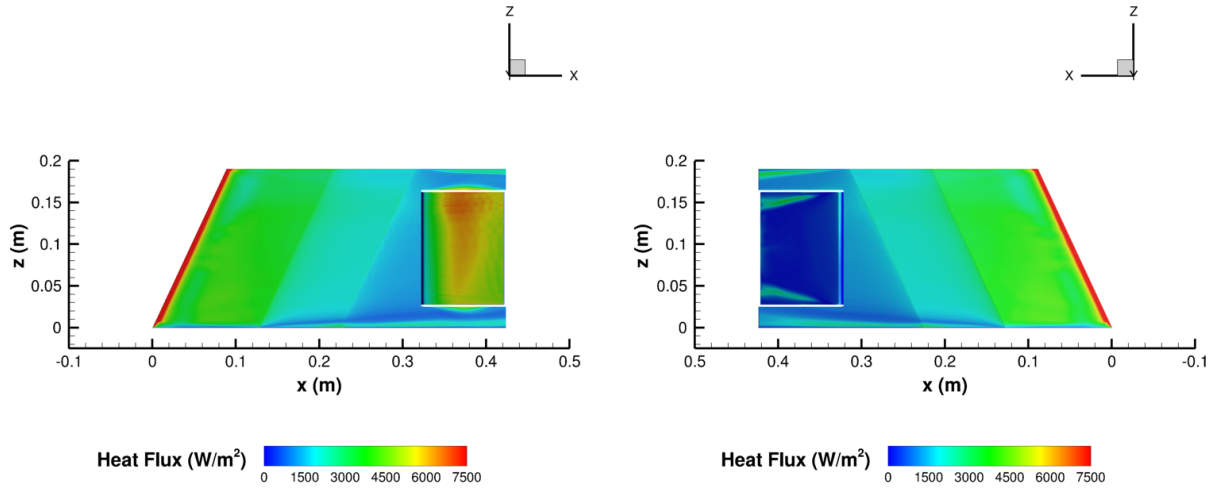

(a) Windward side **(b) Leeward side**

Fig. 7 Surface heat flux contours on the windward and leeward sides of the swept wing-elevon model.

to rise until reaching a peak value around x = 0.37 m. The heat flux on the leeward side of the elevon is comparatively low, except for near the sides where vortex formations produce higher levels of heat flux. The heat flux in the cove is shown close up in Figure 8b. Here, the windward surface is shown with solid lines and the leeward portion is shown with dashed lines. Inside the cove, the heat flux drops significantly, to almost zero near the center. The heat flux on the bottom portion of the elevon shows lower levels of heat flux, with some regions of significantly larger heat flux values that correspond to the formation of the aforementioned vortices.

Figure 9 displays the spanwise surface heat flux distribution inside of the cove and along the elevon surface. Here, solid lines represent the windward surfaces, and dashed lines represent the leeward surfaces. On the left, Figure 9a, the heat flux along the wing-cove surface at 5 different stations, y = 0 m, ± 0.0029 m, and ± 0.0058 m, is displayed. The exact center of the cove is y = 0 m. Near the center of the cove, the heat flux is relatively low, almost near zero. This can be seen for y = 0 and ± 0.0029 m. The heat flux in this region is also mostly constant along the span. At the outer edges of the cove, y = ± 0.0058 m, the heat flux is much higher. The windward portion of the cove experiences flow

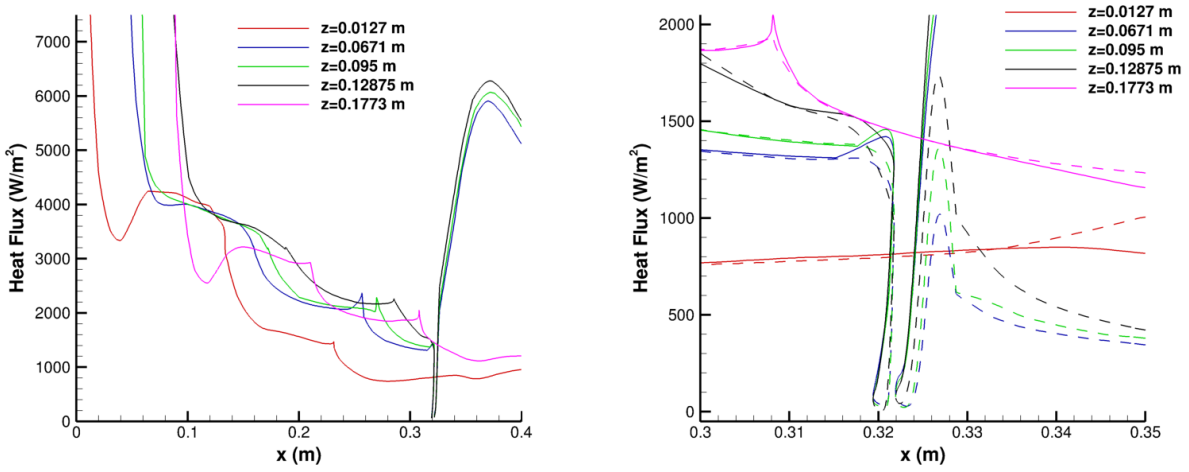

(a) Entire swept wing-elevon model **(b) Local cove region**

Fig. 8 Surface heat flux along various chord-lines of the swept wing-elevon model.

separation, and the leeward side experiences large amounts of flow turning, both displayed in Figure 5a. The heat flux at these locations are less constant, being effected more strongly by the side gaps and three-dimensional flow around the swept wing-elevon. The heat flux is highest near the top side gap. The heat flux distribution along the span of the elevon at various locations is provided in Figure 9b. Once again, the solid lines represent the windward surface and the dashed lines represent the leeward surface. The heat flux distribution is provided for 6 different stations, x = 0.33 m, 0.35 m, 0.37 m, 0.39 m, 0.41 m, and 0.42 m. As shown in this figure, the heat flux distribution on the windward side far exceeds that of the leeward side, with some stations having orders of magnitude difference in values. Starting with the windward side, the first station, x = 0.33 m, is right before reattachment, and shows the lowest levels of heat flux. At the next station, x = 0.35 m, the heat flux jumps in values from the SBLI and boundary layer thinning, and at station x = 0.37 m, the heat flux reaches maximum values. Afterwards, at stations x = 0.39 m, 0.41 m, and 0.42 m, the heat flux distribution along the elevon span starts to decrease in total value. The heat flux along the span of the elevon is relatively constant, however the distribution is asymmetric and tends to increase along the span going towards the wing-tip. This trend is not true for the leeward side of the elevon, shown with the dashed lines. The two large increases in heat flux at the bottom and top of the elevon are attributed to the heat flux streaks mentioned previously. These streaks produce heat flux values that are 2-5 times larger than those near the center-span of the elevon.

C. Vortex Formation

The experimental team ran blockage tests in the Purdue Mach 6 quiet wind tunnel in order to determine allowable model sizing. These tests employed a fixed wing model, without an elevon. During these experiments, they were able to determine that a streak forms on the top portion of the wing surface. This streak is shown below in Figure 10a. Here, temperature-sensitive paint (TSP) is employed. The figure shows a small portion of the top-side of the wing, where the development of a high temperature streak is seen. This streak is produced from the formation of a wing-tip vortex, caused by the low pressure on the trailing-edge edge section of the wing, compared to the freestream pressure, which forces flow downward over the wing-tip. The flow than separates at the sharp edges of the wing-tip and forms a vortex which reattaches on the sides of the wing near the wing-tip [19]. This is similar to the mechanism at which wing-tip vortices are produced [20, 21]; however, the mechanism observed here occurs at zero angle of attack. The computations were able to predict this streak, which is represented in Figure 10b using surface skin friction trajectories and heat flux coloring. These trajectories show the direction of the flow near the wing-tip surface, where the vortex reattaching to the surface creates a diverging line associated with the surface streak. This diverging flow line, created by the wing-tip vortex, produces the high levels of heat flux seen in Figure 10. The experimental photograph provides qualitative validation of the computational results. In addition, RANS computations of the entire wind tunnel with the blockage model (no elevon) were done by Kidambi Sreenivas, who observed the same streak formation [22].

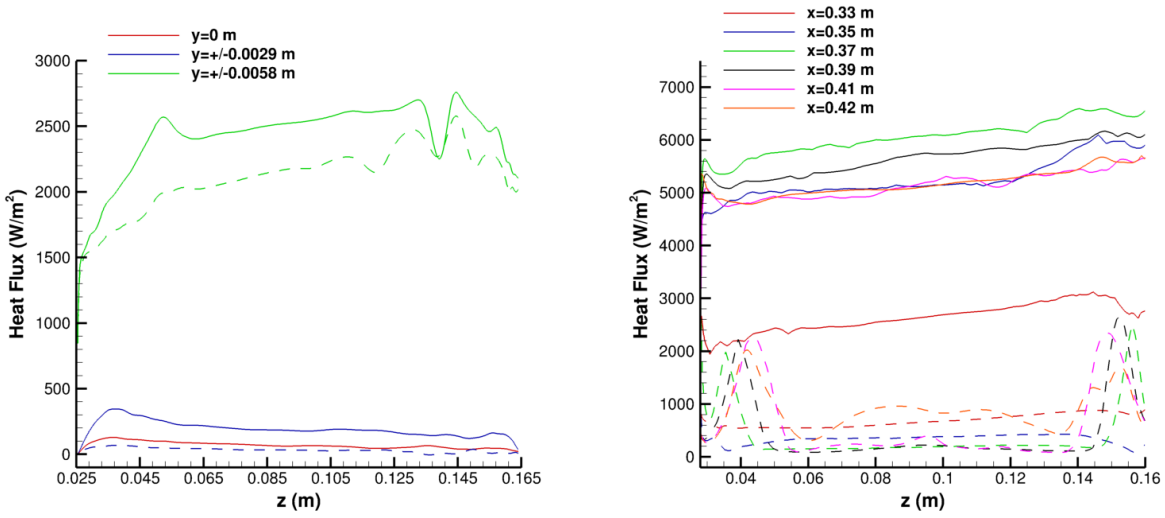

(a) Wing-cove surface **(b) Elevon surface**

Fig. 9 Spanwise surface heat flux distributions in the local cove region and on the elevon surface at various locations.

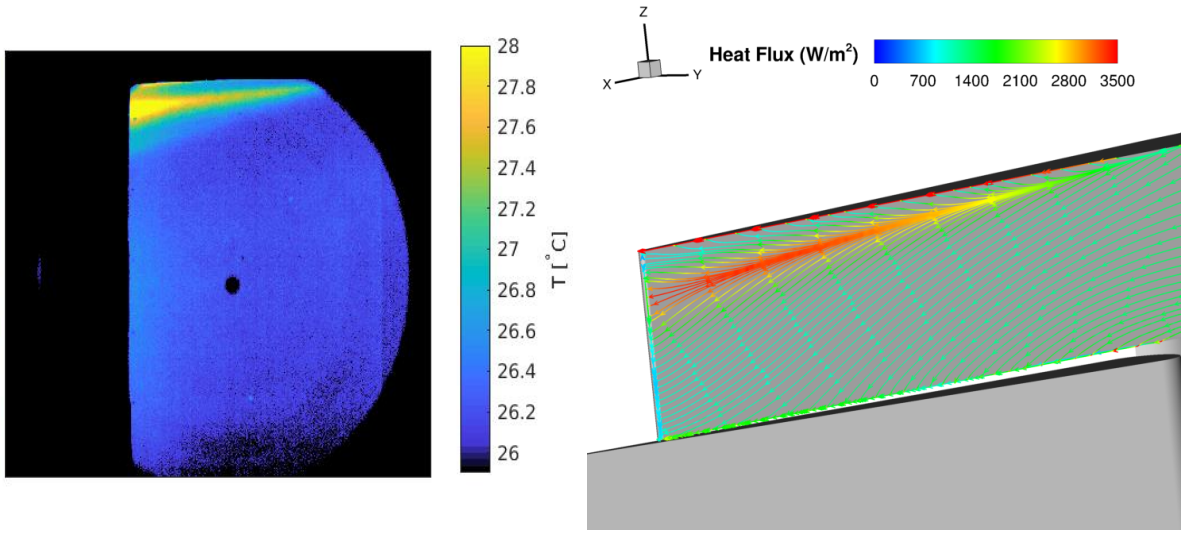

(a) Experimental TSP photograph **(b) Computational skin friction trajectories**

Fig. 10 Comparison between experimental TSP contour from blockage model experiments, without an elevon, and computational data in the same region. Experimental image provided by Carson Lay at Purdue University.

The elevon deflection and complex gap geometry produces more vortices on the leeward surface. The elevon is a lifting surface, and the pressure is higher on the windward side than the leeward side. As a result, spanwise pressure gradients exist which cause flow from the windward side around the tip of the elevon to the leeward side. The concomitant vortex forms primarily on the leeward side, thus the reattachment vortex lines responsible for the streak of high heat flux occurs only on the leeward side. The leeward surface heat flux is visualized in more detail in Figure 11a. Two large vortices are created on the top and bottom portions of the elevon surface, which in turn, create two nearly identical streaks on the elevon surface. These streaks develop as the vortices roll-up and reattach to the elevon surface. The shapes of these streaks are similar to the wing-tip streak, however at the trailing-edge of the elevon they both begin to branch-off. Figure 11b on the right plots the heat flux along the length of the streaks for the two elevon streaks, as well as the wing-tip streak. In this plot, s, represents the running-length of the streak, starting at the beginning of the streak

and ending at the trailing-edge of the wing/elevon, normalized by the length of streak, L_r. The streaks encompass about 70% of the elevon surface. These vortex-induced streaks produce the highest levels of heat flux on the leeward elevon surface, which has been observed for wing-tip vortices [23, 24]. Interestingly, both streaks produce non-similar trends in heat flux. The heat flux along the top elevon streak first increases, reaches a maximum, and then slightly levels off. The bottom elevon streak first increases, reaches a steady level, then increases again toward the elevon's trailing-edge. The top streak, however, produces higher levels of heat flux, more than double at the maximum, than the bottom streak. The wing-tip streak continues to increase along the length of the streak and has the same order of magnitude heat flux as the top elevon streak.

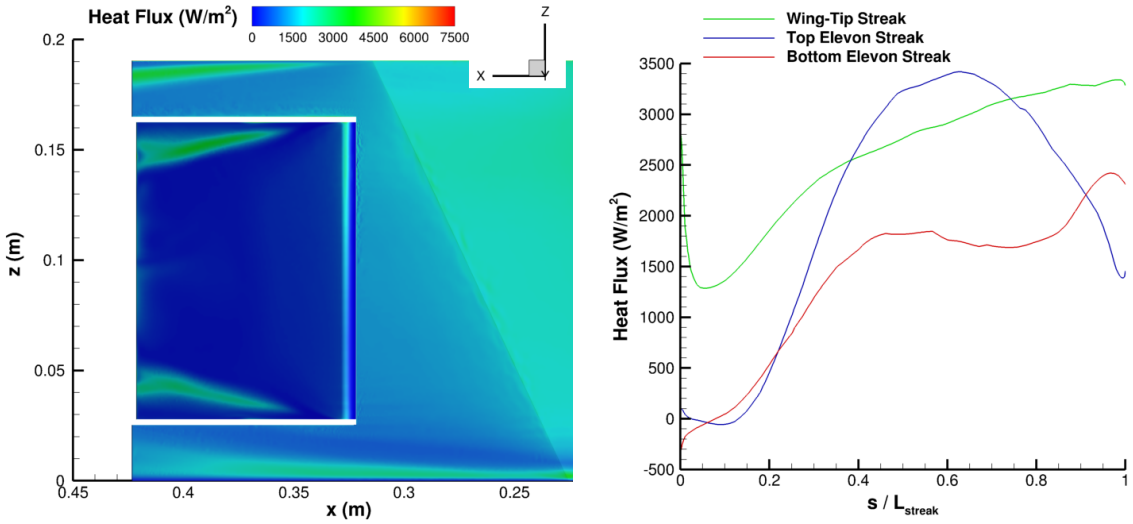

(a) Surface heat flux contour **(b) Surface heat flux along streaks**

Fig. 11 Surface heat flux distribution induced by vortices on the wing-tip and elevon.

The vortices and flow separation are illustrated in Figure 12. The vortex formations are visualized with streamlines colored by Mach number. Here, in Figure 12a, all the major vortices are displayed. The wing-tip vortex is seen as the flow curls around the top portion of the wing and bends down into the wake region of the flow. The top elevon vortex is seen being formed from both flow near the elevon surface and entrainment from the gap regions. The bottom vortex is created with entrainment from flow on the windward and leeward elevon surfaces and the gap regions. This vortex merges with the primary vortex near the wing-root to create one large vortex. This type of vortex merging has been previously observed in wing-tip vortex formations [21]. However, interestingly, the merged vortex seems to produce lower levels of heat flux than the top elevon vortex, as shown in Figure 11b. Downstream of the elevon surface, the flow inside of each of the vortices increases in Mach number. Some portions of the flow inside of the vortices begin to approach freestream Mach numbers.

The complicated flow structure near the leeward elevon surface is depicted in Figure 12b using surface skin friction trajectories colored by heat flux. As with the wing-tip vortex displayed in Figure 10b, the two streaks at the top and bottom of the elevon are clearly seen as divergent lines. The higher levels of heat flux produced by the top elevon vortex are shown with heat flux coloring. As previously mentioned, the heat flux along these streaks is much higher than anywhere else on the leeward elevon surface. The main region of separation is also easily seen with the bifurcating skin friction trajectories in the middle of the elevon surface, which produce a separation region over about 60% of the elevon surface. Along the main diverging bifurcation line, near the two ends of the elevon surface, two nodes are created as an artifact of the oncoming reattaching top and bottom vortices. Near the trailing-edge of the elevon, two additional separation vortex lines can be seen. Figure 12 depicts the intricate nature of the flow near the leeward elevon surface, which in turn, produces flow separation and high levels of heat flux. The behavior of the flow in this region was not necessarily apparent before analysis of the computational data. This visualization may be beneficial in selecting appropriate locations for detailed measurements in the planned experiments.

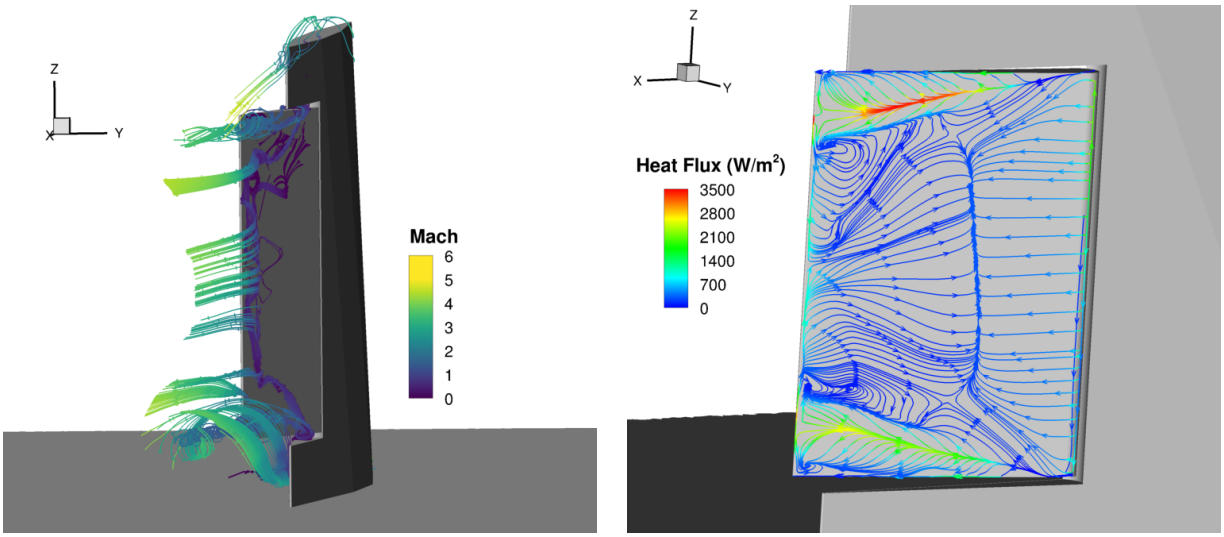

(a) 3-D Streamlines depicting leeward vortex formation

(b) Surface skin friction trajectories

Fig. 12 Intricate vortex formation visualization with use of streamlines, colored by Mach number, and skin friction trajectories, colored by heat flux.

IV. Concluding Remarks

This paper presents computational data for a swept wing-elevon model to be used in upcoming experiments. These data are to be used in part of a joint computational and experimental project at Purdue University, with complementary support with University of Tennessee Space Institute. The purpose of this project is to research high-speed flow past a swept wing-elevon model, focusing on the flow near the cove / gap regions, the intricate vortex formation around the deflected elevon, and the resultant aerothermal loading. The computations done for this research used the software CREATE-AV Kestrel KCFD, employing IDDES to capture the complex flow physics for this configuration. The computational data presented in this paper were time-averaged over 17 ms.

This paper presented data in the following manner. The first portion of data presentation involved visualization of the general flow structure. The fin interaction at the leading-edge of the wing-root was visualized with streamlines, colored via Mach number. The flow around the swept wing-elevon model was displayed with two-dimensional Mach contours in the centerline and center-thickness planes. Flow separation in the cove region and on the trailing-edge elevon were visualized with sectional streamlines. The next portion of the paper focused on aerothermal heating on the swept wing-elevon surface. The three-dimensional swept wing-elevon surface heating was provided with contours of heat flux. The surface heating on the windward and leeward side of the swept wing-elevon surface was then displayed in detail. Heat flux along the chord, including the cove region, was plotted for various spanwise locations. In addition, heat flux along the span of the cove region and on the elevon surface were plotted. The last section focused on the intricate vortex formation on the wing-tip and elevon surface. The wing-tip vortex produced a streak on the top of both sides of the trailing-edge wing surface, which was visualized with skin friction trajectories colored by heat flux. This was compared with an experimental TSP photograph produced by Carson Lay, which showed the same streak formation. The vortex formation on the elevon surface produced two additional streaks, which were visualized with a heat flux contour. The heat flux along the streaks was then plotted. The vortex formations were visualized with streamlines, colored by Mach number. And lastly, the surface flow pattern on the leeward elevon surface was visualized with skin friction trajectories colored by heat flux.

These computations, and the subsequent visualization and analyses done for this paper, are helpful to gain further understanding of this complex flow configuration. While extensive research has been done on fin interactions, shock-wave / boundary-layer interactions, and high-speed airfoil flows, there is limited research on complex geometries that encompass many of these features, such as this swept wing-elevon model. In addition, CFD methods allow us to produce comprehensive data, at relatively low cost comparatively to wind tunnel experiments, to obtain a better understanding of complex flows such as this. The data provided in this paper are also beneficial in order to gain a general understanding of the interesting flow features and to provide sensor-input information for future wind tunnel experiments. For example,

the intricate vortex formation and subsequent trailing-edge separation were not obvious before this computation. As a result, the behavior of this flow is better understood with this research.

Acknowledgments

The present work is supported by the Air Force Research Laboratory under the "Development of Hypersonic Vehicle Flight Test Structures" project, contract number FA8650-19-C-2404. This work is also supported in part by a grant of computer time from the DoD High Performance Computing Modernization Program (HPCMP). The authors would also like to acknowledge Carson Lay, Brandon Chynoweth, and Joseph Jewell from Purdue University, as well as Kidambi Sreenivas from The University of Tennessee at Chattanooga, for their collaboration on this research. This paper, and the contained material, was assigned a clearance of CLEARED (case number AFRL-2021-3898) on 03 Nov 2021. The views expressed in this paper represent the personal views of the authors and are not necessarily the views of the Department of Defense or of the Department of the Air Force.

References

[1] Dolling, D., "Fifty Years of Shock-Wave/Boundary-Layer Interaction Research: What Next?" *AIAA Journal*, Vol. 39, 2001, pp. 1517–1531. doi:10.2514/2.1476.

[2] Bertin, J., and Goodrich, W., "Aerodynamic Heating for Gaps in Laminar and Transitional Boundary Layers," *18th Aerospace Sciences Meeting*, 1980. doi:10.2514/6.1980-287.

[3] Stern, I., and Rowe, W. H., "Effect of Gap Size on Pressure and Heating Over the Flap of a Blunt Delta Wing in Hypersonic Flow." *Journal of Spacecraft and Rockets*, Vol. 4, No. 1, 1967, pp. 109–114. doi:10.2514/3.28818.

[4] Jing, X., Haiming, H., Guo, H., and Song, M., "Numerical Simulation of Supersonic Gap Flow," *PLOS ONE*, Vol. 10, 2015, pp. 1–16. doi:10.1371/journal.pone.0117012.

[5] Cooper, L., and Putz, K. E., "Generalized Flow in Gaps and Slots Including the Effects of Ablation," *Journal of Spacecraft and Rockets*, Vol. 11, No. 5, 1974, pp. 287–294. doi:10.2514/3.62065.

[6] Hunt, L. R., "Aerothermal Environment in Chordwise Gaps Between Split Elevons at Mach 6.8," Tech. Rep. 1783, NASA Langley Research Center Hampton, 1980.

[7] Wong, H., and Kremer, F., "Numerical Assessment on the Heating of the Rudder/Fin Gap in X38 Space Vehicle," *Proceedings of the Third European Symposium on Aerothermodynamics for Space Vehicles*, ESA Special Publication, Vol. 426, 1999, pp. 77–85.

[8] Neumann, R. D., and Hayes, J. R., "Aerodynamic Heating in the Fin Interaction Region of Generalized Missile Shapes at Mach 6," Tech. Rep. 79-3066, Air Force Flight Dynamics Laboratory Wright-Patterson, OH, 1979.

[9] Alviani, R., Poggie, J., and Blaisdell, G., "Detached Eddy Simulation of Supersonic Wing-Elevon Cove Boundary-Layer Ingestion," *AIAA Aviation Forum, AIAA 2020-3008*, June 15-19 2020.

[10] Alviani, R., Poggie, J., and Blaisdell, G., "Unsteady Aspects of Shock-Wave / Boundary-Layer Interaction Resulting from Control Surface Deflection," *AIAA Aviation Forum, AIAA 2021-2823*, August 02-06 2021.

[11] Spalart, P., "Young-Persons Guide to Detached-Eddy Simulation Grids," NASA CR-2001-211032.

[12] Tomaro, R., Strang, W., and Sankar, L., "An Implicit Algorithm for Solving Time Dependent Flows on Unstructured Grids," *35th Aerospace Sciences Meeting and Exhibit*, 1997.

[13] Dolling, D. S., and Bogdonoff, S. M., "Blunt Fin-Induced Shock Wave/Turbulent Boundary-Layer Interaction," *AIAA Journal*, Vol. 20, No. 12, 1982, pp. 1674–1680. doi:10.2514/3.8003.

[14] Houwing, A., Smith, D., Fox, J., Danehy, P., and Mudford, N., "Laminar Boundary Layer Separation at a Fin-Body Junction in a Hypersonic Flow," *Shock Waves*, Vol. 11, 2001, pp. 31–42. doi:10.1007/PL00004055.

[15] Barnhart, P., "Experimental Investigation of Unsteady Shock Wave Turbulent Boundary Layer Interactions About a Blunt Fin," Ph.D. thesis, Case Western Reserve University, Cleveland, Ohio, 1995.

[16] LI, T., and GEIGER, R., "Stagnation Point of a Blunt Body in Hypersonic Flow," *Journal of the Aeronautical Sciences*, Vol. 24, No. 1, 1957, pp. 25–32. doi:10.2514/8.3759.

[17] Reshotko, E., and Cohen, C., "Heat Transfer at the Forward Stagnation Point of Blunt Bodies," Technical Report NACA TN-3513, Lewis Flight Propulsion Laboratory, 1955.

[18] Deveikis, W. D., and Bartlett, W., "Pressure and Heat-Transfer Distributions in a Simulated Wing-Elevon Cove With Variable Leakage at a Free-Stream Mach Number of 6.9," Technical Report NASA TM-74095, Nasa Langley, 1978.

[19] Chynoweth, B., personal communication, July, 2021.

[20] Devenport, W., Rife, M., Liapis, S., Stergios, I., and Follin, G., "The Structure and Development of a Wing-Tip Vortex," *Journal of Fluid Mechanics*, Vol. 312, 1996, p. 67–106. doi:10.1017/S0022112096001929.

[21] Uzun, A., and Hussaini, M., "Simulations of Vortex Formation Around a Blunt Wing Tip," *AIAA Journal*, Vol. 48, No. 6, 2010, pp. 1221–1234. doi:10.2514/1.J050147.

[22] Sreenivas, K., personal communication, June, 2021.

[23] Whitehead, A., and Bertram, M., "Alleviation of Vortex-Induced Heating to the Lee Side of Slender Wings in Hypersonic Flow," *AIAA Journal*, Vol. 9, No. 9, 1971, pp. 1870–1872. doi:10.2514/3.6439.

[24] Alexandrov, S. V., Vaganov, A., and Shalaev, V. I., "Physical Mechanisms of Longitudinal Vortexes Formation, Appearance of Zones with High Heat Fluxes and Early Transition in Hypersonic Flow Over Delta Wing with Blunted Leading Edges," *AIP Conference Proceedings*, Vol. 1770, No. 1, 2016, p. 020011. doi:10.1063/1.4963934.